CrossMark

Effect of Mn doping on structural, optical and magnetic properties of SnO$_2$ nanoparticles

Vivek Agrahari[1] · Anand Kumar Tripathi[1] · Mohan Chandra Mathpal[1,2] ·
Avinash C. Pandey[3] · Sheo Kumar Mishra[4] · R. K. Shukla[4] · Arvind Agarwal[1]

Abstract The Mn doped SnO$_2$ nanoparticles synthesized by cost effective chemical co-precipitation method has been investigated in the present work. The main focus of the work is to explore the structural, optical and magnetic properties of the SnO$_2$ nanostructures. The crystallite size decreases with increase in Mn doping to SnO$_2$ matrix. The optical band gap of doped SnO$_2$ nanoparticles continuously decreases with increasing Mn ion doping concentration. All the doped SnO$_2$ nanoparticles show paramagnetic behavior at room temperature. SnO$_2$ exhibits ferromagnetic behavior in the range of low external applied magnetic field due to the presence of oxygen vacancies (V$_o^+$) and defects. The undoped SnO$_2$ nanoparticles are spherical in shape while Mn doped SnO$_2$ nanoparticles show the segregation of the spherically shaped nanoparticles. Mn ions only enhance the paramagnetic ordering and degrade the ferromagnetism already present in the SnO$_2$ nanoparticle.

✉ Mohan Chandra Mathpal
mohanatnpl@gmail.com

1 Department of Physics, Motilal Nehru National Institute of Technology, Allahabad 211004, India

2 Department of Physics, IIT Bombay, Powai, Mumbai 400076, India

3 Nanotechnology Application Centre (NAC), University of Allahabad, Allahabad 211002, India

4 Department of Physics, University of Lucknow, Lucknow 226007, India

1 Introduction

The wide-band-gap oxide material has renewed and intensified investigations in recent years due to diverse optoelectronic applications by employing their optical transparency in the visible range. It has been investigated that the oxide films have promising applications such as flat-panel displays, gas sensors, high electrical conductivity, protective coatings, light-emitting devices and spintronics devices etc. [1–10]. Tin oxide (SnO$_2$) is known as an n-type wide-band gap (3.6 eV) semiconductor. As an n-type semiconductor, SnO$_2$ shows very high sensitivity towards reducing gases such as H$_2$, CO, hydrocarbon, and alcohol [9–14]. It combines the low electrical resistance with high transparency in visible range and high reflectivity in infra-red range. Tin dioxide (SnO$_2$) possesses several unique properties such as transparency, thermal and chemical stabilities resulting into its numerous optoelectronic applications etc. [3–7]. The optical properties of nanocrystalline semiconductors have been studied extensively in recent years for translating their enhanced properties into practical applications. As the size of the material becomes smaller, it changes the band gap and becomes larger thereby changing the optical and electrical properties of the material and making the material suitable for new applications and devices. Tailoring the physical properties and adding new functionalities to the existing semiconductors by altering the composition, structure, morphology and grain/particle size are the new approaches in advancing the current applications of semiconductor materials. The preparation of such materials in the nanosized range helps in getting increased surface-to-volume ratio which might affect the structural and most other physical properties. The optoelectronic properties such as photoluminescence and optical band gap of SnO$_2$ can also be improved by impurity

doping. The researchers have shown that several dopants (Co, Fe and Cu) can lead to an increase of surface area of SnO_2 by reducing the grain size and crystallinity [15–17]. Various approaches have been adopted for the synthesis of SnO_2 nanoparticles including the hydrothermal method [18, 19], solvothermal method [20], gel-combustion and sol–gel method [21, 22]. Among all these routes the co-precipitation method is an effective way to control the topography and surface properties of metal oxides. In this work the effect of Mn doping on the structural, magnetic and optical properties of SnO_2 nanoparticles prepared by co-precipitation method have been investigated.

2 Experimental procedure

The Mn doped SnO_2 nanocrystalline materials were prepared by the chemical co-precipitation method. All the chemical reagents were used of AR grade and used directly without further purification. In typical synthesis of SnO_2 the stannic tetrachloride hydrated ($SnCl_4 \cdot 5H_2O$); 3.5058 g was dissolved in 100 mL distilled water to prepare 0.1 M solution under vigorous magnetic stirring for 30 min at room temperature. The 4 mL of aqueous ammonia solution was added to the above solution drop wise under stirring to maintain pH in the range of 7–8. The dropping of the solution was well controlled for the chemical homogeneity of the samples. After ageing of 20 h the slurry was filtered and washed around 10 h with distill water to remove impurities from the precipitate. This precipitate was dried in an oven at 70 °C for 10 h to remove water molecules and then calcinated at 400 °C for 2 h in furnace. The calcinations process was started at room temperature. After calcinations the samples were crushed into fine powder to get tin oxide nanomaterials.

For the synthesis of Mn doped SnO_2, the stannic tetra-chloride hydrated ($SnCl_4$ $5H_2O$), 3.5058 g and manganese (II) acetate (IV) hydrate crystal [$(CH_3COO)_2$ Mn $4H_2O$], 0.0245 g (1 at.%) was taken to dissolve in 100 mL distilled water to prepare 0.1 M solution under vigorous magnetic stirring for 30 min. An ammonia solution was added drop wise in this solution under stirring to maintain the pH in between 7 and 8. This process was repeated for 3 at.% (0.0735 g), 5 at.% (0.1225 g), 7 at.% (0.1715 g) and 10 at.% (0.2451 g) of Mn doping. After ageing of 20 h the slurry was filtered and washed out for 10 h with distilled water to remove impurities from the precipitate. This precipitate was then dried in an oven at 70 °C for 10 h to remove water molecules and then calcinated at 400 °C for 2 h in a furnace. The samples were crushed after calcinations into fine powder to get Mn doped tin oxide nanomaterials of different doping concentration. Figure 1 shows

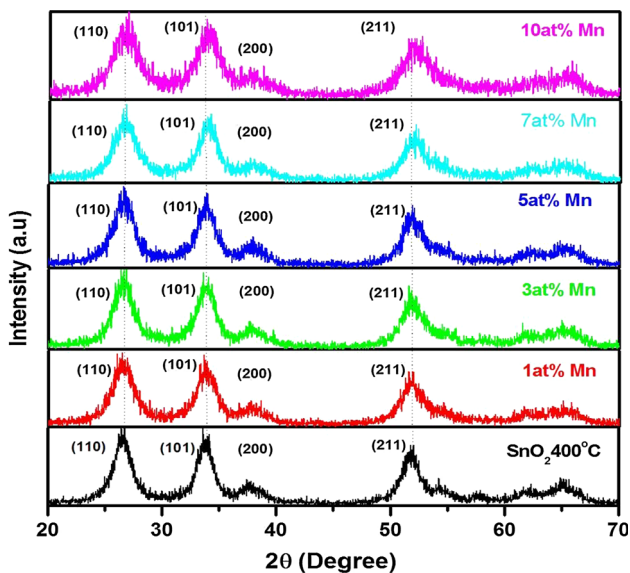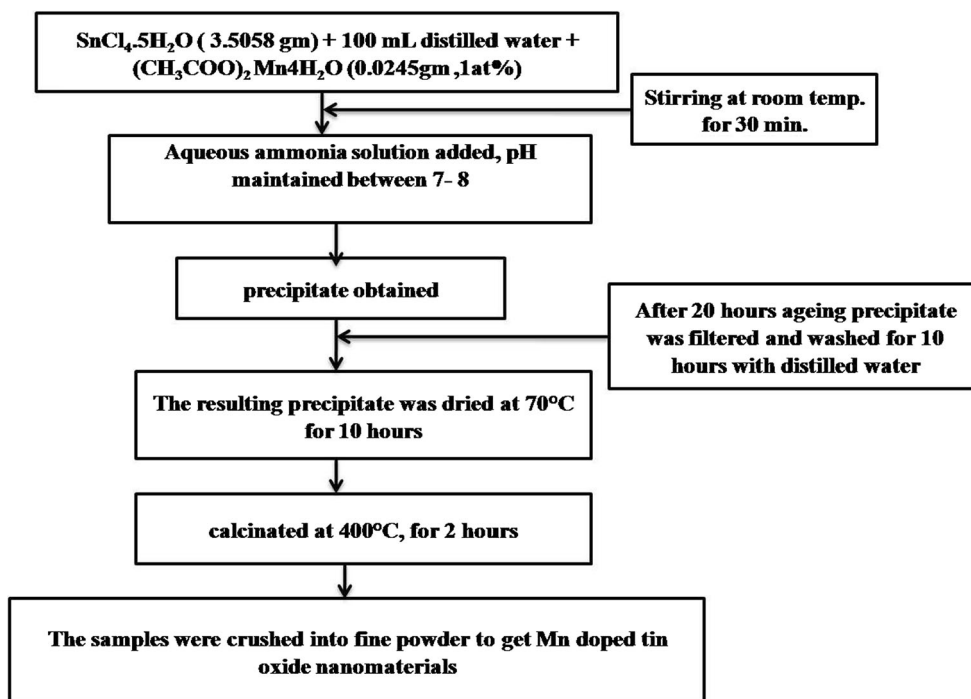the flow chart for the synthesis of Mn doped SnO_2 nanoparticles.

The structural properties of synthesized undoped and Mn doped SnO_2 powder samples were analysed by X-ray diffraction (XRD) measurements using powder diffractometer (Bruker AXS D8) with Cu-Kα radiation ($\lambda = 1.5406$ Å). The size and shape of the synthesized powder were studied by Transmission Electron Microscopy (TEM) measurements using TEM (Hitachi- H-8100). The Fourier Transform Infrared Spectroscopy (FT-IR) spectra of the synthesized samples have been recorded in the spectral range 500–4000 cm^{-1} with Perkin-Elmer 1600 Fourier transform instrument using the KBr pellet technique. The absorption spectra of the samples are taken for the spectral range 250–800 nm with Perkin-Elmer Lambda 35 Ultraviolet Visible (UV–vis) spectrophotometer. The room temperature Raman Spectroscopy (RS) of the powder samples were recorded in the spectra range, 100–1100 cm^{-1} using Thermo Scientific DXR-XI Raman Imaging Microscope. The 532 nm laser line of the Ar^+ ions laser was used to illuminate the powder samples. The photoluminescence emission spectra of the synthesized samples were recorded by using a Spectro-fluorometer (Spex Flurolog3, FL3-22) with a 450 W Xenon Lamp as the excitation source with 330 nm excitation wavelength. For recording the PL spectra, emission slit width was kept to 3.0 nm. The room temperature magnetic properties of the synthesized samples were measured by Vibrating Sample Magnetometer (VSM) (Microsense EV7) measurements.

3 Results and discussion

3.1 X-ray diffraction

Figure 2 represents the powder XRD pattern of pure and 1, 3, 5, 7 and 10 at.% of Mn-doped SnO_2 nanocrystals. Peaks with intensity corresponding to (110), (101) and (211) planes are observed, which indicates that the sample is of high purity with cassiterite SnO_2 structure (JCPDS No. 41-1445). It is clear that there are no extra peaks due to Mn metal oxide implying that the transition metal ion gets substituted at the Sn site without changing the structure. The Table 1 illustrates that the crystallite size reduces from 5.6 to 3.1 nm for doped SnO_2 nanoparticles. It is revealed that as the Mn doping concentration increases from 1 % to 10 at.% the presence of Mn ions in SnO_2 prevented the growth of crystal grains. This suggest that Mn ions are incorporate into the lattice in the form of Mn^{3+} (radius 0.065 nm) or Mn^{+4} (radius 0.054 nm), as the ionic radius of Mn in these two states is smaller than the ionic radii of Sn^{+4} (0.070 nm) [23].

Fig. 1 Flow chart for synthesis of Mn doped SnO$_2$ nanoparticles

SnCl$_4$.5H$_2$O (3.5058 gm) + 100 mL distilled water + (CH$_3$COO)$_2$Mn4H$_2$O (0.0245gm ,1at%)

Stirring at room temp. for 30 min.

Aqueous ammonia solution added, pH maintained between 7– 8

precipitate obtained

After 20 hours ageing precipitate was filtered and washed for 10 hours with distilled water

The resulting precipitate was dried at 70°C for 10 hours

calcinated at 400°C, for 2 hours

The samples were crushed into fine powder to get Mn doped tin oxide nanomaterials

Fig. 2 XRD of the samples calcinated at 400 °C

There is an increase in crystallinity in the Mn doped metal oxide SnO$_2$ nanoparticles when compared to the pure SnO$_2$ nanoparticles. This physical process suggest that a portion of the metal oxide ions forms stable solid solution with SnO$_2$ and the metal oxide ions occupy the regular lattice site in SnO$_2$. This will introduce the point defects and change in stoichiometry owing the charge imbalance, which may induce the distortion in crystal structure of the host compound. If metal ions occupy the regular lattice site in SnO$_2$, then the interference takes place between Mn-doped metal ions and those of SnO$_2$ lattice and thus the crystallinity of the doped nanoparticles tends to enhance than that of pure SnO$_2$ nanoparticles.

3.2 Scanning electron microscope and transmission electron microscope

Figure 3 shows the overall surface morphology of pure and doped SnO$_2$ nanoparticles. It is observed from that pure SnO$_2$ compound consists of large agglomeration than doped SnO$_2$. The SEM investigations of all the samples reveal the crystallites nature of nanoparticles. The TEM images are depicted in Figs. 4, 5 and 6 which illustrates that the nanoparticles are spherical in shape. The doped SnO$_2$ shows clusteration of spherically shaped nanoparticles. The selected area electron diffraction (SAED) indicates that polycrystalline nature of the samples. It shows that the crystallinity increases with increase in Mn content.

The interplanar spacing calculated for different sets of planes is approximately same as for the main peaks observed in the XRD pattern. The estimated d-spacing for (110) plane is 0.335 nm. The average particle size was calculated from particle size distribution curve shown in Fig. 7a–c. The calculated average particle size is 7.8 ± 0.3, 6.3 ± 0.4 and 7.5 ± 0.4 nm for undoped SnO$_2$, 1 and 5 at.% Mn doped SnO$_2$ nanoparticles respectively. Particle size calculated from TEM images is comparable with the calculated crystallite size from the XRD. In general the particles observed from TEM images are likely to contain a single or several primary crystallite grains which

Table 1 Lattice parameters and crystallite size of the samples

S. No.	Samples	Lattice parameter (Å)	Average crystallite size (nm)
1	SnO$_2$ 400 °C	a = b = 4.784 c = 3.211	5.6
2	1 at.% Mn	a = b = 4.806 c = 3.223	4.9
3	3 at.% Mn	a = b = 4.699 c = 3.204	3.7
4	5 at.% Mn	a = b = 4.780 c = 3.178	3.6
5	7 at.% Mn	a = b = 4.682 c = 3.253	3.2
6	10 at.% Mn	a = b = 4.646	3.1
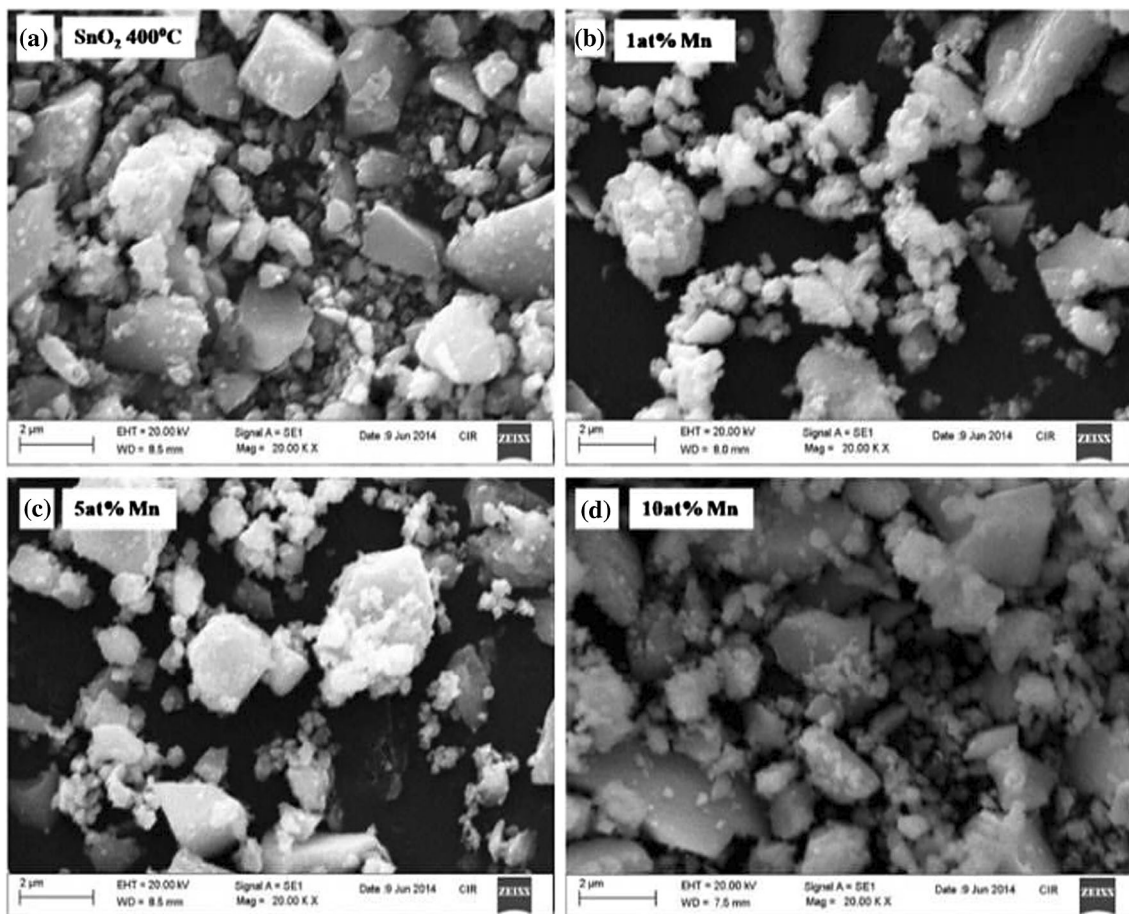
Fig. 3 SEM images of Mn-doped SnO$_2$ nanoparticles at 2 μm scale

are measured in terms of average mean crystallite size by XRD.

3.3 Optical properties

Absorption and fluorescence spectroscopy are powerful nondestructive techniques to explore the optical properties of semiconducting nanoparticles. In order to determine the optical band gaps and associated properties, the optical absorbance measurement were carried out at room temperature and the absorbance of pure and Mn doped SnO$_2$ nanoparticles are shown in Fig. 8. The absorbance is expected to depend on several factors such as band gap, impurity centers, vacancies and surface roughness [24]. Absorbance spectra exhibit an absorption peak at around 280 nm which can be attributed to the photo excitation of

Fig. 4 **a** TEM image and **b** SAED pattern of un-doped SnO$_2$
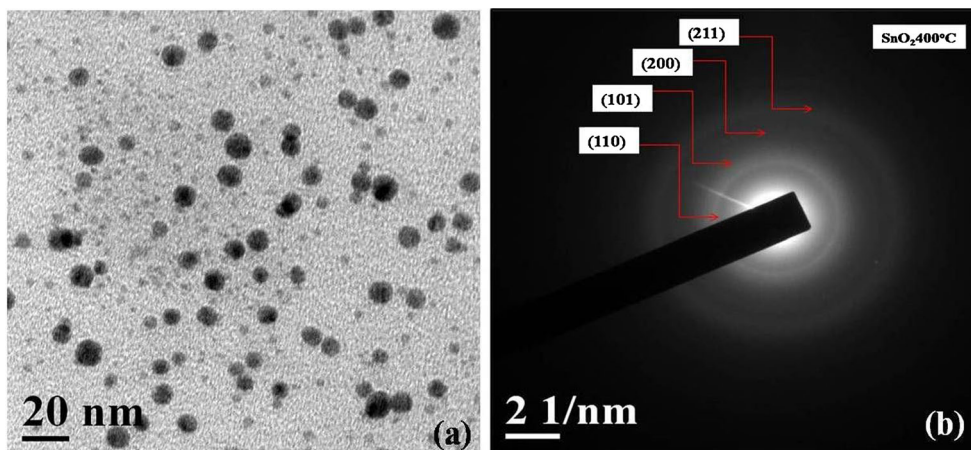
Fig. 5 1 at.% Mn-doped SnO$_2$ **a** TEM image and **b** SAED pattern
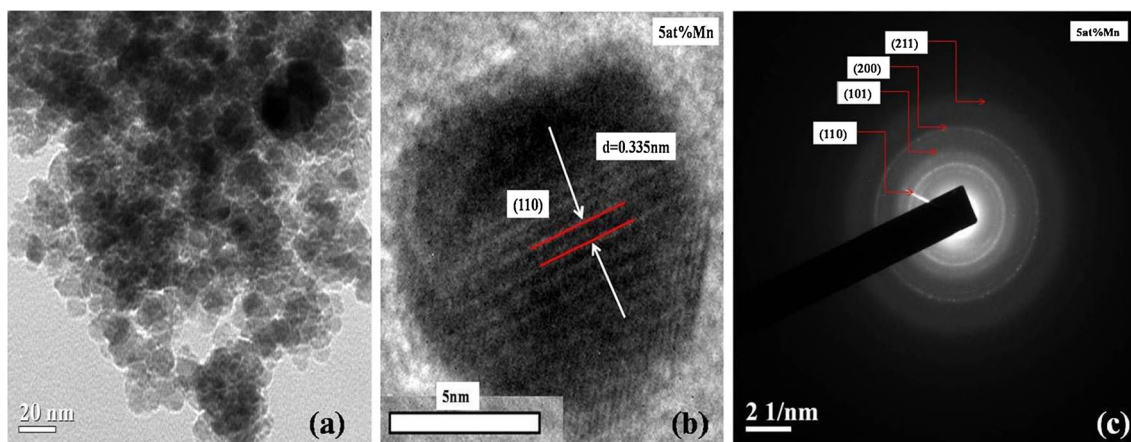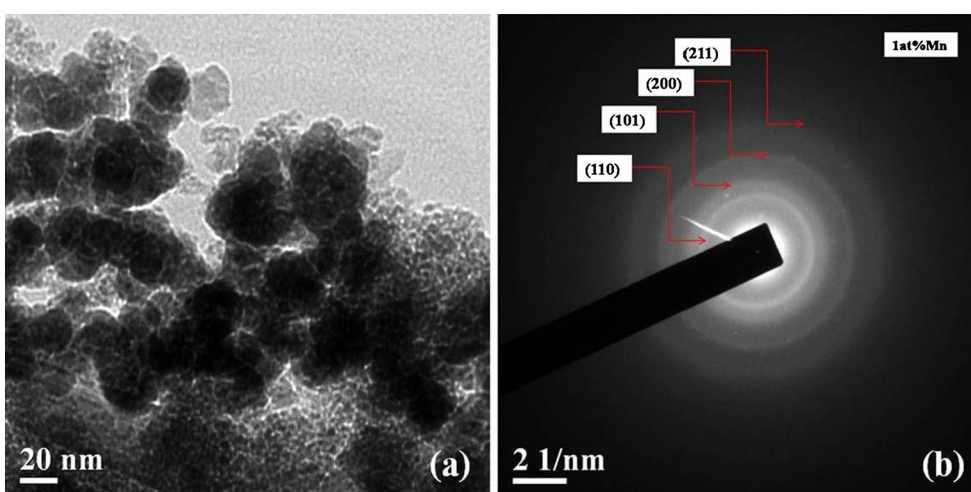
Fig. 6 5 at.% Mn-doped SnO$_2$ **a** TEM image, **b** HRTEM image and **c** SAED pattern

electrons from valence band to conduction band. The absorption edge of different samples varies as the concentration of Mn doping in the SnO$_2$ nanoparticles. It can be seen that the absorbance tends to increase with the increase in dopant concentration.

Tauc plots as shown in Fig. 9 were used to calculate the direct band gap by using the Tauc relation:
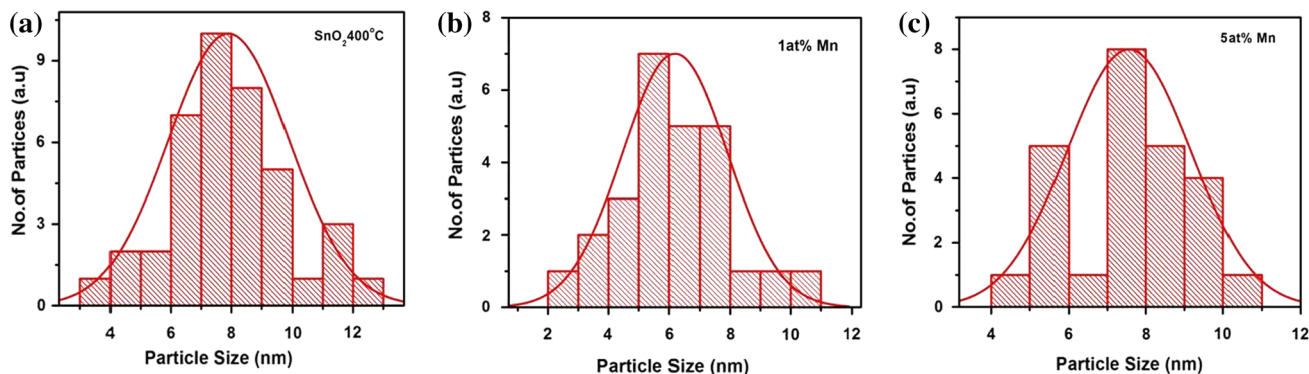
$$\alpha h\upsilon = A\left(h\upsilon - E_g\right)^n$$

Fig. 7 Particle size distribution curve; **a** SnO_2, **b** 1 at.% Mn doped SnO_2 and **c** 5 at.% Mn doped SnO_2
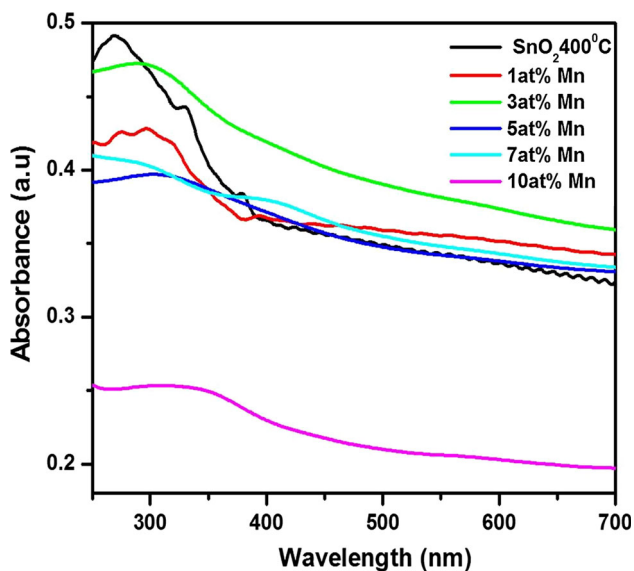

Fig. 8 Optical absorption spectra of the samples

where α is the absorption coefficient, A is a constant. n = 1/2 for direct band gap semiconductors. The linear region in the plot of $(\alpha h \nu)^2$ versus $h\nu$ can be extrapolated to calculate the value of the optical band gap E_g. The measured band gap was found to be 2.81 eV for undoped SnO_2 nanoparticles (Table 2), which is lower than the reported value of the bulk SnO_2 (3.6 eV). The spectra of Mn doped SnO_2 nanoparticles display red shift in the band gap with increasing the dopants amount. The similar shift was observed by other researcher by incorporation of metal ions into SnO_2 nanoparticles [25–27]. This Red shift can be assigned to the charge-transfer transitions between the metal ions d-electrons and the SnO_2 conduction or valence band [28].

3.4 FT-IR analysis

FT-IR spectra of the samples are shown in the Fig. 10. It is observed that there are clear changes in the positions and

sizes of IR peaks indicating that Mn has incorporated into SnO_2 host matrix. The band observed at 670 cm^{-1} may be assigned to the antisymmetric Sn–O–Sn stretching mode. The band in the region 480–510 cm^{-1} can be attributed to symmetric Sn–O–Sn and Mn–O bonds. The peak appearing at 1120 cm^{-1} is related to the vibration of hydroxyl-tin (Sn–OH) bond. The vibration band observed at 1380 cm^{-1} can be assigned to N–O symmetric stretch for the existence of nitro based compounds due to synthesis from nitrates precursors in the samples while the peak at 1694 cm^{-1} is assigned to C=O stretching vibration. The present assignments corroborate well with the values reported in available literature [29, 30]. The prominent bands around 3800 and 1630 cm^{-1} account for the presence of absorbed molecular water.

3.5 Photoluminescence

Photoluminescence (PL) is a useful tool for investigating the optical properties of undoped and doped semiconductor nanostructures. The doped nanostructures are expected to have different optical properties in comparison to undoped nanostructures. Figure 11 shows the photoluminescence (PL) spectra of undoped and Mn doped SnO_2 nanoparticles. The PL spectra of the synthesized samples are obtained as a result of the competition among electron–hole separations, electron–phonon scattering and electron–hole recombination. The band edge emissions centered in the range of 393–396 nm can be attributed to the V_o related defects, mainly singly ionized oxygen vacancy (F^+ center or V_o^+) defects which are believed to be recombination of excitons for all the samples [31]. The PL spectra exhibits a broad emission edge in the range of 400–500 nm which is the indication for the presence of multiple peaks under a main peak corresponding to multiple emissions from oxygen vacancies present in these samples. These vacancies thus generates the defect levels in the crystal and enhances the visible emission in the spectra [24, 32].
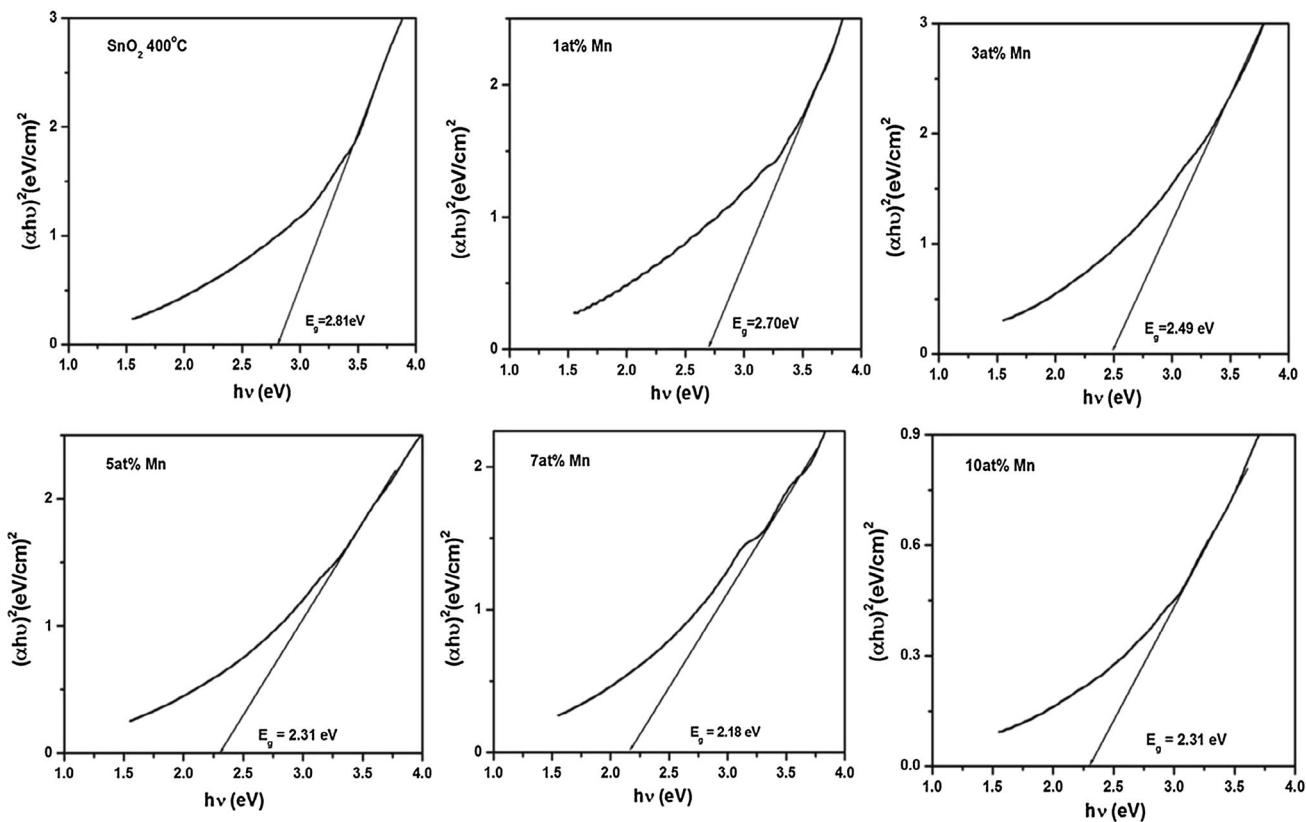
Fig. 9 Tauc plot of the samples

Table 2 Absorption edges and energy band gap of all the samples

Mn concentration (at.%)	Wavelength (nm)	Energy band gap (eV)
0	441	2.81
1	460	2.70
3	498	2.49
5	537	2.31
7	569	2.18
10	537	2.31

3.6 Raman spectra

Figure 12 shows the Raman spectra for undoped and Mn doped SnO_2 nanoparticles within the range 100–1100 cm^{-1}. SnO_2 having tetragonal rutile crystalline structure with point group D_{4h}^{14} and space group P4$_2$/mnm consist of the six unit cell atoms which give a total of 18 branches for the vibration modes in the first Brillouin's zone. The representation of the vibration modes at the center of the Brillouin's zone is given as [33]:

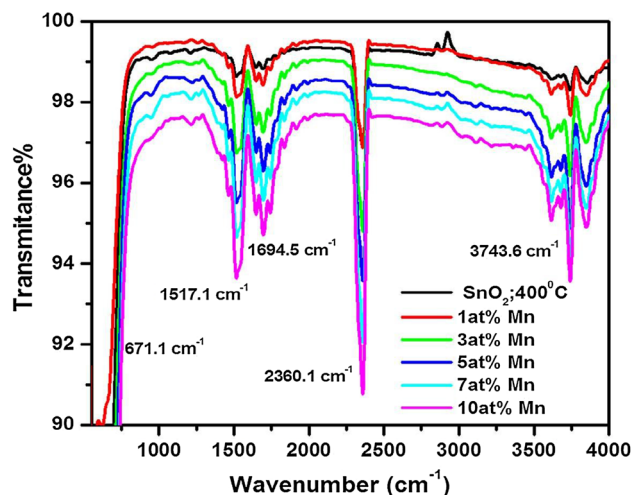$$\Gamma = 1A_{1g} + 1A_{2g} + 1A_{2u} + B_{1g} + 1B_{2g} + 2B_{1u} + 1E_g + 3E_u$$

Fig. 10 FT-IR spectra of SnO_2 and Mn doped SnO_2 samples

where the B_{1g}, E_g, A_{1g}, and B_{2g} modes of SnO_2 are Raman active. Here E_u and A_{2u} bands are infrared (IR) active, and A_{2g} and B_{1u} are silent or inactive to both Raman and IR. One A_{2u} and two E_u modes are acoustic. In the Raman active modes Sn atoms remain at rest while oxygen atoms
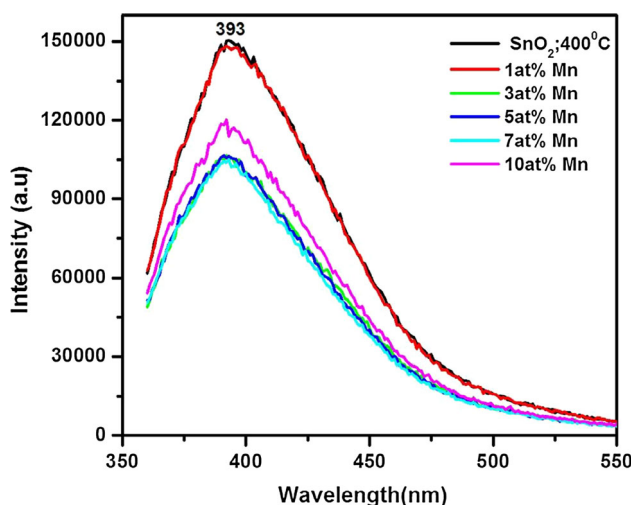
Fig. 11 PL spectra of all the samples

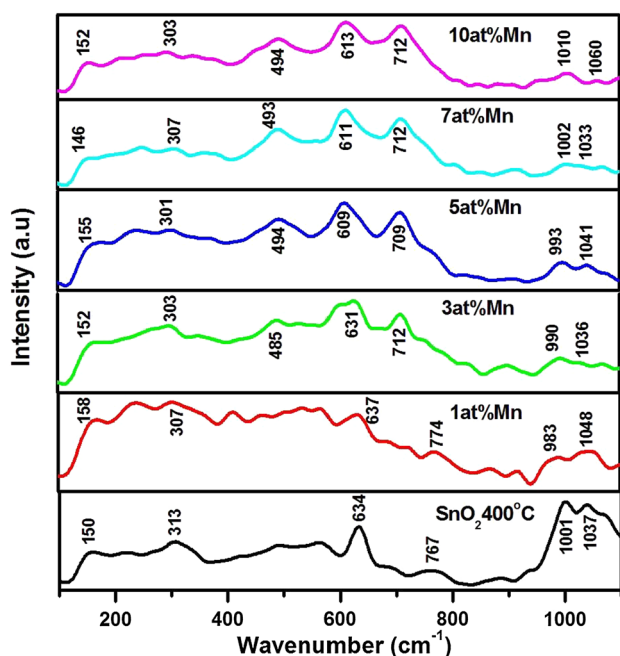**Fig. 12** Raman spectra of all the samples

vibrate. The Raman bands of the pure rutile phase SnO_2 were observed in different range of the Raman spectra. The broad band centered in the range of 485–494 cm^{-1} for all the samples is assigned to E_g band. The vibrational band in the range of 609–637 cm^{-1} is the most fundamental mode of vibration of rutile phase of SnO_2 and assigned to A_{1g}. The third fundamental mode of vibration for undoped and 1 at.% doped SnO_2 is found in the range of 767–774 cm^{-1} and is attributed to B_{2g}. The A_{1g} and B_{2g} modes are non degenerate and might be related to the expansion and contraction of the vibrating mode of Sn–O bonds, whereas the doubly degenerate E_g mode may be related to the

vibration of oxygen in the oxygen plane. The B_{2g} and A_{1g} modes present in the spectra vibrate in the plane perpendicular to the c-axis, while the E_g mode always vibrates in the direction of the c-axis. The gradual changes in the Raman spectra has been observed with the increase of 3 at.% Mn doping in the SnO_2 lattice which may be attributed to the strong electron–phonon interaction in the system. Few new Raman bands in the low wavenumber region (140–315 cm^{-1}) with a very low intensity can be observed in most of the samples which are associated with the surface modes of SnO_2 nanostructures. Additional peaks in the range of 983–1060 cm^{-1} can be observed in all the samples, which can be assigned to laser-excited luminescence due to presence of defects in SnO_2 nanoparticles [32–34].

3.7 Magnetic properties

The field dependent magnetization [M(H) at 300 K] measurement of SnO_2 and Mn (1, 5 and 10 at.%) doped SnO_2 nanocrystalline samples calcinated at 400 °C are shown in Fig. 13. The graph is magnified in the central region (in the region −2500 to 2500 Oe) and is shown in Fig. 13b. All the measurements shown here have been corrected by eliminating the signals from the sample holder. All curves clearly exhibit hysteresis behavior and magnetization under a strong externally applied magnetic field of 20 KOe. The Mn (1, 5 and 10 at.%) doped SnO_2 graph exhibits paramagnetism at room temperature under an externally applied magnetic field of 20,000 Oe. The undoped SnO_2 nanoparticles exhibit ferromagnetism with low coercivity and positive susceptibility only for externally applied lower magnetic field region of −2500 to 2500 Oe. The maximum coercivity (∼450 Oe) was observed for undoped SnO_2 which decreases gradually for Mn doped SnO_2 nanocrystalline samples.

The SnO_2 nanoparticles exhibit diamagnetic behavior for an externally applied magnetic field of higher than 2500 Oe. The coercivity and positive susceptibility may be associated with the exchange coupling of the spins of electrons trapped in oxygen vacancies (V_o), which are mainly present on the surface of the SnO_2 nanoparticles and the surface defects created during synthesis process as evident from PL spectra also. The literature reveals that these oxygen vacancies basically located on the particle surface are considered to play a key role for the paramagnetism and ferromagnetism in nanosized SnO_2 [35–41]. Unpaired electrons can be trapped in those oxygen vacancies and their spins can polarize together via exchange interactions and lead to ferromagnetic order in SnO_2 nanoparticles [35]. As the strength of externally applied magnetic field is increased the magnetic susceptibility continuously increases for Mn doped SnO_2
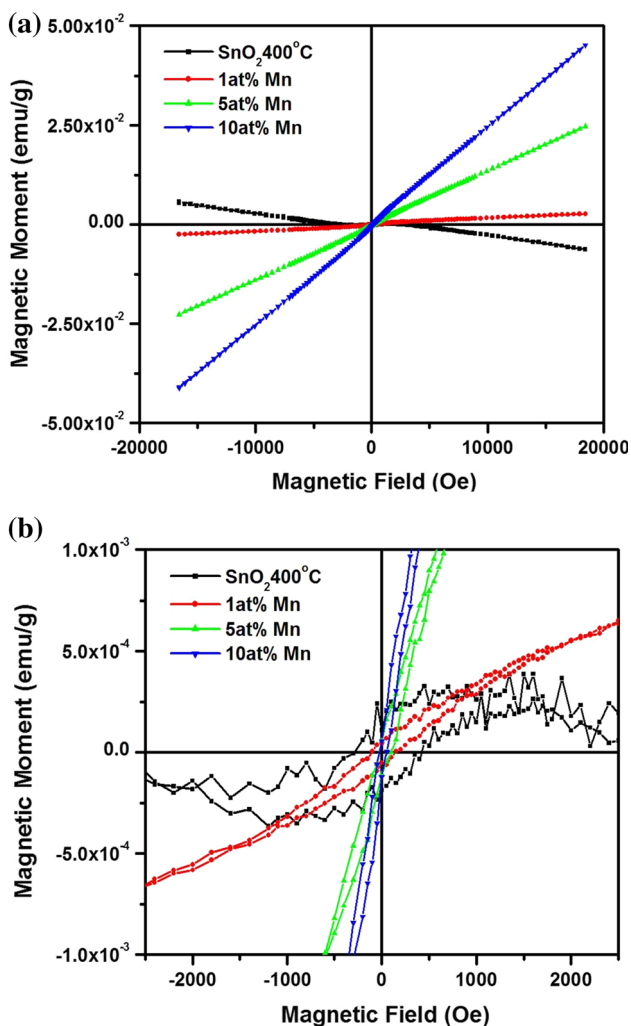
Fig. 13 a M–H plot of SnO_2 and Mn doped (1, 5 and 10 at.%) SnO_2 nanoparticles and **b** magnified graph

nanoparticles and consequently the graphs show paramagnetic nature for all the doped samples. The similar existence of paramagnetic and ferromagnetic moments has been reported previously by other researchers in pure and doped SnO_2 [32, 35–42]. The graphs illustrates that as the Mn dopants concentration increases the particles becomes more aligned in the direction of applied magnetic field as the net magnetic moment increases after Mn doping. These results strongly suggest that the magnetic order observed in the Mn doped SnO_2 nanoparticles is intrinsic in nature. Therefore the main role of the Mn cations is not to originate the magnetic ordering; rather it only modifies the paramagnetism and degrades the ferromagnetism already present in the SnO_2 nanoparticles. Beside this the presence of extrinsic impurities or paramagnetic phases with concentrations well below the detection limit of the instruments can be responsible for the enhanced paramagnetic signals observed at room temperature [39–42]. Further investigations are required to understand such room

temperature magnetic behavior of undoped and doped SnO_2 based DMS nanostructures. Magnetic and optical properties of different RE and transition metals (TM's) doped SnO_2 nanoparticles of different particle shape and sizes are currently understudy and will be published elsewhere in future.

3.8 Time resolved photoconductivity rise and decay measurement

The time-resolved rise and decay photocurrent spectrum helps in understanding the photoconductivity dynamics of materials when the light is abruptly switched on and off. The rise and decay of photocurrent spectrum can be useful in determining the nature of recombination centers present inside the materials. The time-resolved rise and decay at room temperature for the photocurrent spectrum of the undoped and doped SnO_2 nanoparticles under visible illumination of 370 nm are shown in Fig. 14. The prepared SnO_2 nano particles are n-type semiconductors due to oxygen vacancies and other native defects. Such vacancies and defects serve as active sites for the adsorption of oxygen and H_2O molecules. The surface related mechanism, which is governed by desorption and adsorption processes plays an important role in the photoconductivity properties of the nano structures due to large surface-to-volume ratio [43]. The graph shows when the field is applied, the initial dark current is high in most of the samples. This is attributed for the presence of oxygen vacancies at the surface and other native defects acting as donors as well as the process of adsorption of water molecules, thus releasing the charge carriers. Thereafter, the dark current starts decreasing and attains its minimum value. The reduction in the dark current is rapid in SnO_2 as compared to the doped SnO_2 nanoparticles. The anomalous behavior in time resolved photoconductivity may be attributed to the presence of an additional hydroxyl group as generally the decrease in the conductivity is due to the field-induced adsorption of oxygen from air [44]. As the illumination of light is switched off, electron–hole recombination process dominates, so the conductivity decreases in all the samples. The trap depth value was calculated to be 0.69, 0.68, 0.66, 0.65, 0.67 and 0.66 eV for pure and 1, 3, 5, 7 and 10 at.% of Mn-doped SnO_2 nanoparticles respectively [31]. Trap depth is maximum for undoped sample indicates that the higher energy is required to remove an atom from the trap as compared to the other samples.

Kumar et al. [45] have reported the growth and decay of the photocurrent generation in Cu–Ni nanoparticle-decorated r-graphene hybrid nano-composite (Cu–Ni GrHNC). In their study they also observed similar results that initially the increase in photocurrent is very fast with a time
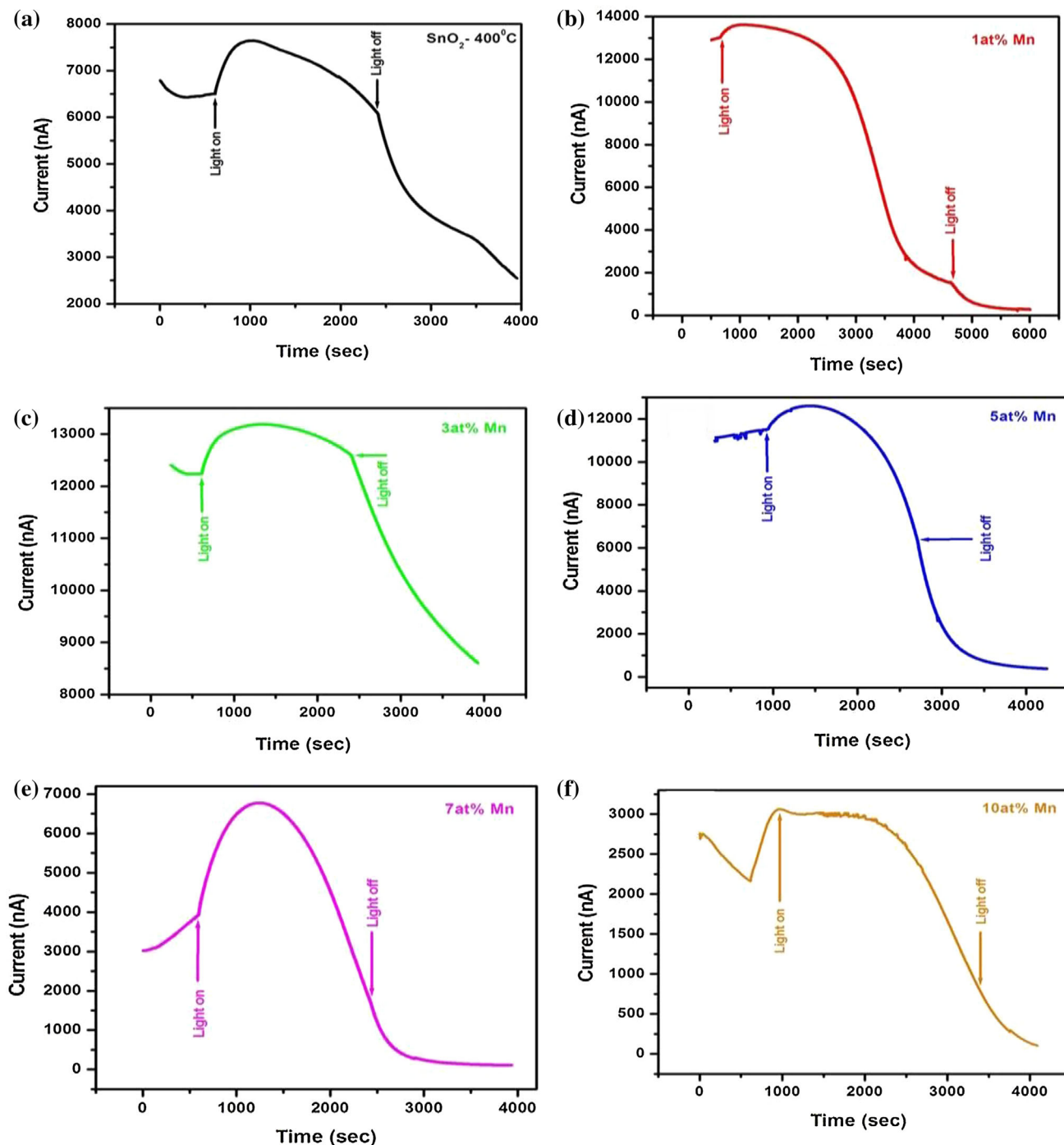
Fig. 14 Time resolved rise and decay photoconductivity measurement for the samples

constant of 0.84 s, and then growth becomes slow with a time constant of 31.73 s and finally it gets saturated. As the power is switched off, a fast decay in the current with decay time constant of 2.2 s was observed, which further keep decreasing with a slower decay time constant of 93.19 s. In our case the growth and decay time constants are slow as compared to Kumar et al. results. These slow

photoconductive rise and decay response may be attributed to a large amount of recombination centers and presence of trap levels and defect states within the band gap [46, 47]. Srivastava et al. [46] reported the similar photo response properties for variation in Cu dopant concentration on ZnS nanoparticles synthesized by co-precipitation method. The photocurrent initially found to increase in all Cu doped ZnS

samples due to fast process of generation of electron–hole pairs (EHPs) as a result of absorption of photons. For the un-doped (ZnS) sample, photocurrent increases up to maximum value and then starts decreasing slowly even during illumination. Such kind of negative photoconductivity (NPC) is caused by the presence of imperfection centers in the forbidden gap as observed in our case also [46]. Maurya et al. [47] reported the photoconducting behavior in rutile TiO_2 synthesized by simple hydrolysis method at low calcination temperatures of 80 and 450 °C. The observed trap depth value in their case was 0.65 and 0.69 eV for TiO_2 samples calcinated at 80 and 450 °C respectively. These results are in good agreements with the trap depth value calculated in our case for Mn doped SnO_2 nanoparticles.

4 Conclusion

Mn doped SnO_2 nanoparticles were synthesized by a simple chemical co-precipitation method. The rutile phase tetragonal crystal structure of doped SnO_2 nanostructures was confirmed from XRD, HRTEM and SAED analysis. Crystallite size decreases with increase in Mn doping concentration in SnO_2 nanostructures. The SnO_2 nanoparticles are spherical in shape while the doped SnO_2 crystallites show clusteration of spherically shaped nanoparticles. The optical band gap of undoped SnO_2 nanoparticles was calculated to be 2.81 eV and it decreases continuously with the increase of Mn doping in SnO_2. The room temperature ferromagnetism in SnO_2 nanoparticles due to the presence of defects and oxygen vacancies has been observed while the Mn doped SnO_2 nanoparticles exhibit room temperature paramagnetism. The strong optical absorption with weak magnetic properties at room temperature may serve the nanomaterials as a potential candidate for many spintronics, optoelectronics and DMS based applications.

References

1. S. Ferrere, A. Zaban, B.A. Gregg, J. Phys. Chem. B **101**, 4490 (1997)
2. S.G. Ansari, P. Boroojerdian, S.R. Sainkar, R.N. Karekar, R.C. Aiyer, S.K. Kulkarni, Thin Solid Films **295**, 271 (1997)
3. R.W.J. Scott, S.M. Yang, G. Chabanis, N. Coombs, D.E. Williams, G.A. Ozin, Adv. Mater. **13**, 1468 (2001)
4. A. Teeramongkonrasmee, M. Sriyudthsak, Sens. Actuators, B **66**, 256 (2000)
5. G. Feng, S.F. Wang, M.K. Lu, Y.X. Qi, G.J. Zhou, D. Xu, D.R. Yuan, Opt. Mater. **25**, 59 (2004)
6. V. Subramanian, K.I. Gnanasekar, B. Rambabu, Solid State Ionics **175**, 181 (2004)
7. Y. Idota, T. Kubota, A. Matsufuji, Y. Maekawa, T. Miyasaka, Science **276**, 1395 (1997)
8. M.C. Mathpal, A.K. Tripathi, P. Kumar, R. Balasubramaniyan, M.K. Singh, J.S. Chung, S.H. Hur, A. Agarwal, Phys. Chem. Chem. Phys. **16**, 23874 (2014)
9. S.B. Ogale, R.J. Choudhary, J.P. Buban, S.E. Lofland, S.R. Shinde, S.N. Kale, V.N. Kulkarni, J. Higgins, C. Lanci, J.R. Simpson, N.D. Browning, S. Das Sarma, H.D. Drew, R.L. Greene, T. Venkatesan, Phys. Rev. Lett. **91**, 077205 (2003)
10. J.M.D. Coey, A.P. Douvalis, C.B. Fitzgerald, M. Venkatesan, Appl. Phys. Lett. **84**, 1332 (2004)
11. N.H. Hong, J. Sakai, W. Prellier, A. Hassini, J. Phys.: Condens. Matter **17**, 1697 (2005)
12. G.Z. Zang, J.F. Wang, H.C. Chen, W.B. Su, C.M. Wang, P. Qi, J. Phys. D Appl. Phys. **38**, 1072 (2005)
13. M.M.B. Mohagheghi, M.S. Saremi, Semicond. Sci. Technol. **19**, 764 (2004)
14. A.C. Bose, P. Thangadurai, S. Ramasamy, Mater. Chem. Phys. **95**, 72 (2006)
15. H. Jin, Y. Xu, G. Pang, W. Dong, Q. Wan, Y. Sun, S. Feng, Mater. Chem. Phys. **85**, 58 (2004)
16. J. Hays, A. Punnoose, R. Baldner, M.H. Engelhard, J. Peloquin, K.M. Reddy, Phys. Rev. B **72**, 075203 (2005)
17. G. Korotcenkov, V. Macsanov, V. Brinzari, V. Tolstoy, J. Schwank, A. Cornet, J. Morante, Thin Solid Films **467**, 209 (2004)
18. H. Zhu, D. Yang, G. Yu, H. Zhang, K. Yao, Nanotechnology **17**, 2386 (2006)
19. F. Du, Z. Guo, G. Li, Mater. Lett. **59**, 2563 (2005)
20. Y. Liu, F. Yang, X. Yang, Colloids Surf. A **312**, 219 (2008)
21. L. Fraigi, D.G. Lamas, N.E.W. Reca, Nanostruct. Mater. **11**, 311 (1999)
22. S.V. Manorama, C.V.G. Reddy, V.J. Rao, Nanostruct. Mater. **11**, 643 (1999)
23. Z.M. Tian, S.L. Yuan, J.H. He, P. Li, S.Q. Zhang, C.H. Wang, Y.Q. Wang, S.Y. Yin, L. Liu, J. Alloys Compd. **466**, 26 (2008)
24. A.S. Ahmed, M. Muhamed Shafeeq, M.L. Singla, S. Tabassum, A.H. Naqvi, A. Azam, J Lumin **131**, 1 (2011)
25. T. Takagahara, K. Takeda, Phys. Rev. B **46**, 15578 (1992)
26. W. Choi, A. Termin, M.R. Hoffmann, J. Phys. Chem. **98**, 13669 (1994)
27. C. Wang, D.W. Bahnemann, J.K. Dohrmann, Chem. Commun. **16**, 1539 (2000)
28. Z.J. Li, B. Hou, Y. Xu, D. Wu, Y.H. Sun, J. Mater. Sci. **40**, 3939 (2005)
29. J.J. Zhu, J.M. Zhu, X. Liao, J. Fang, M. Zhou, H. Chen, Mater. Lett. **53**, 12 (2002)
30. P.G. Harrison, A. Guest, J. Chem. Soc., Faraday Trans. **183**, 3383 (1987)
31. A.K. Tripathi et al., Mater. Sci. Semicond. Process. **23**, 136–143 (2014)
32. S. Ghosh, G.G. Khan, K. Mandal, ACS Appl. Mater. Interfaces **4**, 2048–2056 (2012)
33. A. Dieguez, A.R. Rodriguez, A. Vila, J.R. Morante, J. Appl. Phys. **90**, 1550 (2001)
34. J. Yu, L. Cui, H. He, S. Yan, Y. Hu, H. Wu, J. Rare Earths **32**, 1 (2014)
35. F.H. Aragon, J.A.H. Coaquira, P. Hidalgo, S.L.M. Brito, D. Gouvea, R.H.R. Castro, J. Phys. Condens. Matter. **22**, 496003 (2010)
36. C. Wang, M. Ge, J.Z. Jiang, Appl. Phys. Lett. **97**, 042510 (2010)
37. G.A. Alanko, A. Thurber, C.B. Hanna, A. Punnoose, J. Appl. Phys. **111**, 07C321 (2012)
38. V. Agrahari, M.C. Mathpal, M. Kumar, A. Agarwal, J. Alloy. Compd. **622**, 48 (2015)

39. M. Subramanian, P. Thakur, S. Gautam, K.H. Chae, M. Tane-mura, T. Hihara, S. Vijayalakshmi, T. Soga, S.S. Kim, K. Aso-kan, R. Jayavel, J. Phys. D Appl. Phys. **42**, 105410 (2009)
40. M.H. Choi, T.Y. Ma, Mater. Lett. **62**, 1835 (2008)
41. P. Mohanapriya, R. Pradeepkumar, N.V. Jaya, T.S. Natarajan, Appl. Phys. Lett. **105**, 022406 (2014)
42. S. Dhar, O. Brandt, M. Ramsteiner, V.F. Sapega, K.H. Ploog, Phys. Rev. Lett. **94**, 037205 (2005)
43. J.S. Jie, W.H. Zhang, Y. Jiang, X.M. Meng, Y.Q. Lie, S.T. Lee, Nano Lett. **6**, 1887–1892 (2006)
44. D.H. Zhang, D.E. Brodie, Thin Solid Films **261**, 334–339 (1995)
45. A. Kumar, S. Husale, A.K. Srivastava, P.K. Dutta, A. Dhar, Nanoscale **6**, 8192 (2014)
46. R.K. Srivastava, N. Pandey, S.K. Mishra, Mater. Sci. Semicond. Process. **16**, 1659–1664 (2013)
47. A. Maurya, P. Chauhan, S.K. Mishra, R.K. Srivastava, J. Alloy. Compd. **509**, 8433–8440 (2011)